Flow in a wavy-walled channel lined with a poroelastic layer

By H. H. WEI[1], S. L. WATERS[2], S. Q. LIU[3]
AND J. B. GROTBERG[1]

[1]Department of Biomedical Engineering, University of Michigan, Ann Arbor, MI 48109, USA

[2]Division of Applied Mathematics–Theoretical Mechanics, School of Mathematics Science, University of Nottingham, Nottingham, NG7 2RD, UK

[3]Department of Biomedical Engineering, Northwestern University, Evanston, IL 60208

Motivated by physiological flows in capillaries, venules and the pleural space, the pressure-driven flow of a Newtonian fluid in a two-dimensional wavy-walled channel is investigated theoretically. The sinusoidal wavy shape is due to the configuration of underlying cells, their nuclei and intercellular junctions or clefts. The walls are lined with a thin poroelastic layer that models the glycocalyx coating of the cell surface. The upper and lower wavy walls are offset axially by the phase angle Φ, where $\Phi = 0$ (π) yields an antisymmetric (symmetric) channel. Biphasic theory is employed for the poroelastic layer and the flow is solved by a lubrication approximation using a small parameter, $\delta \ll 1$, where δ is the channel width/wavelength ratio. The velocity fields in the core and layer are determined as perturbation expansions in δ^2 and finite-Reynolds-number effects occur at $O(\delta^2)$ assuming $\delta^2 Re \ll 1$. When the hydraulic resistivity, α, the ratio of the channel width to the Darcy permeability, is sufficiently large and Φ is near enough to π, the flow develops a trapped recirculation eddy within the glycocalyx layer near the widest part of the channel. This can be of significance to transport through the cellular boundary, since that location corresponds to intercellular clefts through which important fluid and solute exchange occurs. Increasing $|\Phi - \pi|$ diminishes the recirculation region. Increasing the Reynolds number moves the recirculation slightly upstream. Both layer velocity and wall shear stresses decrease as α increases and support the appearance of flow recirculation. Further, the wavy geometry allows a portion of the flow to enter and exit the layer, which provides a mechanism for convective transport between these two regions that otherwise have only diffusive interactions. The relevant Péclet number is $Pe = V_n^* b / D$ where D is molecular diffusivity and V_n^* is the normal velocity to the glycocalyx layer. For large molecules, $Pe = O(10^2)$ or higher, so the convective transport is important. The solid displacement, dictated by the layer flow field, increases as α increases.

1. Introduction

Transport in and across capillary blood vessels and intrapleural membranes plays an essential role in maintaining metabolism and fluid balance of surrounding tissues. A fundamental question in understanding the flow behaviour in this *in vivo* environment is related to the role of the thin fibre matrix layers that coat the cells. One of the most important of these layers for blood vessels is the endothelial glycocalyx that uniformly coats the luminal surface of the vascular endothelium. It consists of oligosaccharide

chains covalently bound to membrane protein, lipids and polysaccharide chains of integral membrane proteoglycan molecules. Plasma proteins such as fibrinogen and albumin, can also be adsorbed and thus contribute to the fibre matrix of macro-molecules that comprise the glycocalyx. The thickness of the layer has been estimated to vary from 0.1 μm *in vitro* (Adamson & Clough 1992) to 0.4–0.5 μm *in vivo* (Vink & Duling 1996), or even more than 1 μm by estimating microvascular flow resistance (Pries *et al.* 1997). From a hydrodynamic point of view, this layer can be regarded as a hydrated gel with fibre volume fraction between 1% and 2% (Weinbaum, Tsay & Curry 1992). This extracelluar layer also provides a selectively permeable barrier to the passage of macromolecules from the blood to the extracellular space. To serve this function, the fibre space must at least sieve albumin and other plasma proteins, which implies the interfibre distance, $\Delta \leqslant 7$ nm (Weinbaum 1998). This has been strongly supported by the experiments of Henry & Duling (1999).

The presence of the surface glycocalyx has drawn attention to work on capillary haemodynamics and red cell motion. It is well known that haematocrit in capillaries is much lower than systemic haematocrit. However, it is only partly accounted for by the Fahraeus effect (Fahraeus 1928). It is now believed that a reduction of haematocrit in capillaries can be reasonably explained by taking account of the glycocalyx (Pries *et al.* 1997), as earlier proposed by Desjardins & Duling (1987). There are numerous theoretical studies in this area. Most earlier models treated red cells as either rigid or deformable pellets moving in a straight capillary without accounting for the presence of a porous layer (Wang & Skalak 1969; Tozeren & Skalak 1978; Secomb *et al.* 1986). To account for the interaction between red blood cells and the porous layer, Wang & Parker (1995) and Damiano *et al.* (1996) applied lubrication and binary mixture theory (Mow *et al.* 1980) to describe the motion of rigid particles in a tube coated by a porous layer. Damiano (1998) and Secomb, Hsu & Pries (1998) have extended their model to a deformable cell moving within the core fluid, but the former also included analysis of a flow in a coated-layer capillary without red blood cells. They all showed that flows are significantly retarded by the porous layer. Feng & Weinbaum (2000) developed a more general lubrication theory to account for a highly compressible porous layer, a result of red blood cell penetration into the glycocalyx. They showed that there is a much greater repulsive force than that predicted by classical lubrication theory. Their model can explain recent experimental measurements for the apparent viscosity of blood (Pries *et al.* 1994). As such, the influence of the glycocalyx layer on haemodynamics in a straight capillary has been appreciated. However, the vessel wall is made of endothelial cells whose shape is typically non-uniform along the vessel. It is therefore essential to characterize the effects of wall geometry on the flow field.

We should first understand how wavy geometry changes flow patterns. There are numerous studies for steady flows over wavy boundaries. We focus primarily on flows with low Reynolds numbers that are applicable to microvascular systems. We are particularly interested in the flow-separation phenomenon induced by uneven boundaries because it is critical to mass transport. Pozrikidis (1987) numerically investigated a pressure-driven Stokes flow in a wavy channel, and showed that the flow can separate and form a recirculation in the widest part of the channel, depending on parameters such as channel width, wavelength and amplitude of the wavy wall. Clearly, larger channel width, shorter wavelength or large amplitude make flow separation more feasible. Flow separation occurs when a local adverse pressure gradient induced by local variations of the geometry is strong enough to reverse flow so that the corresponding wall shear stress or vorticity changes sign. It is worth noticing that boundary or shear-driven flows have a greater likelihood of separation

even in a nearly parallel channel (Middleman 1998). This is because no external driving force is available to overcome a gradually developing adverse pressure when the flow passes a wider part of the channel (Pozrikidis 1987).

Since free-surface or two-phase flows bear some hydrodynamic similarities to the flow in a capillary blood vessel, it is also instructive to see the effect of a wavy boundary on such flow systems for understanding the mechanism of flow separations. For a free-surface flow down a wavy inclined plane (Pozrikidis 1988), a flow recirculation occurs in the wall valley for a sufficiently large liquid thickness or high flow rate. A study of core–annular flow of two immiscible fluids in a tube of slowly varying cross-section (Kouris & Tsamopoulos 2000) showed that there is flow separation in the annular region at sufficiently large Re. This critical value of Re decreases when the core to annulus viscosity ratio is reduced.

Flow separation is possible for flow in porous media. A study of fluid motions in the glycocalyx layer driven by moving red cells demonstrated that low permeability enhances the degree of flow recirculation (Feng & Weinbaum 2000). As mentioned earlier, the characteristics of the wall geometry are a deterministic factor in causing flow separation. The effects of waviness and the glycocalyx layer have been studied by Waters, Liu & Grotberg (1997) and by Secomb, Hsu & Pries (2002). The latter analysis includes the presence of moving deformable red blood cells in wavy capillaries with the glycocalyx layer. The results in Secomb *et al.* (2002) suggest that the presence of the glycocalyx layer reduces the impact of wall waviness on flow resistance. However, it is not clear how the wall waviness affects the flow even in the absence of red blood cells, particularly for the region between two adjacent red blood cells. In this case, it is necessary to consider the coupling of the luminal flow to the glycocalyx layer. This coupling can change the flow patterns and stress distributions, which in turn may influence molecular transport and cellular response.

The present study excludes the presence of red blood cells and can be regarded as modelling the flow regions between them. When red cells are present, the pressure distribution along the cell surface, which is in close proximity to the capillary wall, depends on the free-stream pressure in the region we are modelling. In addition, our model is also applicable to the flow in the pleural space of the lung. We consider a simplified two-dimensional model of the blood vessel lined with the wavy endothelium whose surface is coated by the glycocalyx layer, a poroelastic medium of uniform thickness. We shall follow the approach by Damiano *et al.* (1996) and Wang & Parker (1995) and employ biphasic mixture theory (see the Appendix) to describe the poroelastic medium. By assuming small aspect ratio of the mean channel width to the wavelength (i.e. size of an endothelial cell), we shall apply lubrication theory to the motion of both core and layer fluids and demonstrate how the presence of the glycocalyx couples to the wall variation to affect flow patterns, particularly for flow separation.

2. Governing equations and boundary conditions

Consider the steady flow of two fluids in a two-dimensional wavy channel (see figure 1). The top and bottom channel walls are located at $y^* = B_1^*(x^*) = b(1 + a \cos(2\pi/Lx^*))$ and $y^* = B_2^*(x^*) = -b(1 + a \cos(2\pi/Lx^* - \Phi))$, respectively. The channel has a mean width of b. The channel wall has an amplitude of ba and a wavelength of L. The top and bottom walls have a phase difference of Φ. A poroelastic glycocalyx layer with a uniform thickness ϵb lines the wall. Therefore, the permeable interfaces are located at $y^* = H_i^*(x^*) = B_i^*(x^*) + (-1)^i \epsilon b$, $i = 1, 2$ for the top and bottom portions. The core
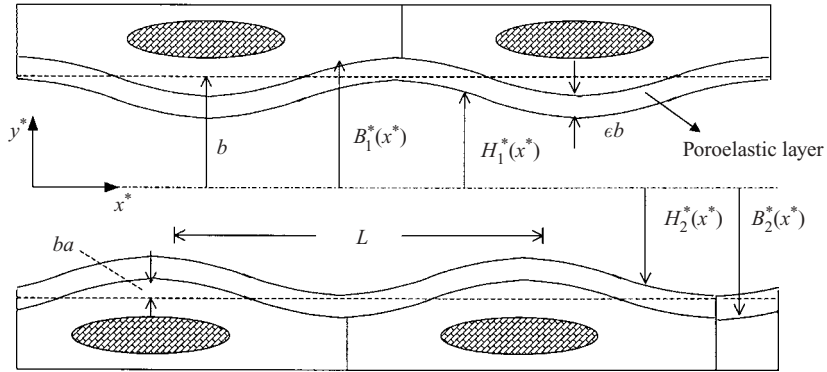
FIGURE 1. Wavy-walled channel with a uniformly thick poroelastic layer.

is a Newtonian fluid with viscosity μ_1 and occupies the region $H_2(x^*) \leqslant y^* \leqslant H_1(x^*)$. The fluid with viscosity μ_2 flows within the poroelastic layers $H_1^*(x^*) \leqslant y^* \leqslant B_1^*(x^*)$ and $B_2^*(x^*) \leqslant y^* \leqslant H_2^*(x^*)$. Both fluids are assumed to have the same density ρ.

We now scale x^* and y^* by L and b, respectively. Let Q be the characteristic volumetric flow rate per unit depth into the channel. Then axial and vertical velocity scales are Q/b and Q/L, respectively. The pressure is then scaled by $\mu_1 QL/b^3$. Let $\delta = b/L$ be the aspect ratio of the channel and define the Reynolds number to be $Re = \rho QL/\mu_1 b$. For the core we denote (U, V, P) to be the axial and vertical velocities and the pressure, respectively. The resulting dimensionless governing equations for the core are:

$$U_x + V_y = 0, \tag{2.1}$$

$$\delta^2 Re(UU_x + VU_y) = -P_x + U_{yy} + \delta^2 U_{xx}, \tag{2.2}$$

$$\delta^4 Re(UV_x + VV_y) = -P_y + \delta^2 V_{yy} + \delta^4 V_{xx}. \tag{2.3}$$

The poroelastic layer consists of fluid and solid phases. According to biphasic theory (Mow *et al.* 1980) (also see the Appendix), the velocities of the solid phase are generally non-zero and couple to those of the fluid phase. However, for a steady state, the solid velocities should be zero. As such, for the fluid phase, let (u, v, p) be the axial and vertical velocities and the pressure, respectively, then the dimensionless governing equations (see (A 1) and (A 2) in the Appendix) for the fluid phase with zero solid velocities become

$$u_x + v_y = 0, \tag{2.4}$$

$$\alpha^2 u = -\frac{\phi}{m} p_x + u_{yy} + \delta^2 u_{xx}, \tag{2.5}$$

$$\alpha^2 \delta^2 v = -\frac{\phi}{m} p_y + \delta^2 v_{yy} + \delta^4 v_{xx}. \tag{2.6}$$

Here, ϕ is the volume fraction of the fluid in the poroelastic layer and $m = \mu_2/\mu_1$ is the viscosity ratio of the core to the layer fluids. The dimensionless hydraulic resistivity α is defined in terms of K_p the Darcy permeability parameter:

$$\alpha = \frac{b}{\sqrt{K_p}}, \tag{2.7}$$

which is assumed to remain constant. As a result, the flow field of the fluid phase is uncoupled from the solid phase. It is worth noting that the forms of (2.5) and (2.6) are Brinkman-type equations (Brinkman 1947). For the solid phase, the axial and vertical displacements are scaled by δ and $b\delta$. Let (u^s, v^s) be the corresponding dimensionless displacements, then the governing equations (see (A 5) in the Appendix) for the solid displacements are,

$$-\alpha^2 u = -\frac{1-\phi}{m}p_x + \eta u^s_{yy} + \delta^2 u^s_{xx} + \eta(\chi + 1)\delta^2\left(u^s_{xx} + v^s_{xy}\right), \qquad (2.8)$$

$$-\alpha^2\delta^2 v = -\frac{1-\phi}{m}p_y + \eta\delta^2\left(v^s_{yy} + v^s_{yy}\right) + \eta(\chi + 1)\delta^2\left(v^s_{yy} + u^s_{xy}\right), \qquad (2.9)$$

where $\chi = \lambda_s/\mu_s$ is the ratio of the Lamé coefficient λ_s to the shear modulus μ_s of the solid phase and $\eta = \mu_s b^2/\mu_2 Q$. The left-hand sides of (2.8) and (2.9) are the results of neglecting the solid phase velocity. As a result, the solid displacements are dictated by the flow field of the fluid phase, and they can be obtained once the flow field is known.

Let the subscript $i = 1, 2$ denote the top and the bottom portions of the flow geometry, respectively. Then, the system is subject to the following boundary conditions. The fluid velocities vanish on the walls at $y = B_i(x)$,

$$u = 0, \quad v = 0. \qquad (2.10)$$

There are no solid displacements along the walls at $y = B_i(x)$,

$$u^s = 0, \quad v^s = 0. \qquad (2.11)$$

The boundary conditions at the core–layer interface (Hou *et al.* 1989) can be approximately applied at the stationary interface because of a small-deformation assumption for the poroelastic layer. At the interface $y = H_i(x)$, the effective forms of continuous velocity across the permeable interfaces (see (A 6) and (A 7) in the Appendix) yield

$$U = \phi u, \quad V = \phi v. \qquad (2.12)$$

The stress conditions at the core–layer interfaces (see (A 9)–(A 11) in the Appendix) are as follows. The tangential stress conditions $y = H_i(x)$ are

$$\phi\left(\left(1 - \delta^2 H_{i_x}^2\right)(U_y + \delta^2 V_x) + 2\delta^2 H_{i_x}(V_y - U_x)\right)$$
$$= m\left(\left(1 - \delta^2 H_{i_x}^2\right)(u_y + \delta^2 v_x) + 2\delta^2 H_{i_x}(v_y - u_x)\right). \qquad (2.13)$$

Similar stress conditions at $y = H_i(x)$ applied between the core and the solid phase of the layer yield

$$(1 - \phi)\left(\left(1 - \delta^2 H_{i_x}^2\right)(U_y + \delta^2 V_x) + 2\delta^2 H_x(V_y - U_x)\right)$$
$$= m\eta\left(\left(1 - \delta^2 H_{i_x}^2\right)\left(u^s_y + \delta^2 v^s_x\right) + 2\delta^2 H_{i_x}\left(v^s_y - u^s_x\right)\right). \qquad (2.14)$$

Finally, the normal stress conditions at $y = H_i(x)$ give

$$\phi\left(-P + 2\frac{\delta^2}{1 + \delta^2 H_{i_x}^2}\left(V_y - H_{i_x}(U_y + \delta^2 V_x) + \delta^2 H_{i_x}^2 U_x\right)\right)$$
$$= -\phi p + 2m\frac{\delta^2}{1 + \delta^2 H_{i_x}^2}\left(v_y - H_{i_x}(u_y + \delta^2 v_x) + \delta^2 H_{i_x}^2 u_x\right). \qquad (2.15)$$

3. Lubrication approximation

With the governing equations and boundary conditions as above, we now begin to solve the flow fields. We assume that the axial variation of the wavy wall is small, i.e. $\delta \ll 1$, this allows us to employ lubrication theory. As such, we can expand the flow quantities in a perturbation series for small δ:

$$\left.\begin{aligned}
(U, V, P) &= (U_0, V_0, P_0) + \delta^2(U_1, V_1, P_1) + \dots, \\
(u^i, v^i, p^i) &= \left(u_0^i, v_0^i, p_0^i\right) + \delta^2\left(u_1^i, v_1^i, p_1^i\right) + \dots, \\
(u^{is}, v^{is}) &= \left(u_0^{is}, v_0^{is}\right) + \delta^2\left(u_1^{is}, v_1^{is}\right) + \dots.
\end{aligned}\right\} \tag{3.1}$$

The superscript $i = 1, 2$ denotes the top- and the bottom-layer regions. The first-order correction is δ^2, since no terms of order δ appear in the governing equations and boundary conditions. The following subsections are the results of substituting (3.1) into (2.1)–(2.15) and collecting quantities of similar order in δ.

3.1. *The leading-order problem*

For the core flow at the leading order in δ, by assuming $Re = O(1)$, the governing equations (2.1)–(2.3) become

$$U_{0_x} + V_{0_y} = 0, \tag{3.2}$$

$$0 = -P_{0_x} + U_{0_{yy}}, \tag{3.3}$$

$$0 = -P_{0_y}. \tag{3.4}$$

For the fluid phase of the layer, we omit superscripts i for brevity and the leading-order governing equations (2.4)–(2.6) are

$$u_{0_x} + v_{0_y} = 0, \tag{3.5}$$

$$\alpha^2 u_0 = -\frac{\phi}{m} p_{0_x} + u_{0_{yy}}, \tag{3.6}$$

$$0 = -\frac{\phi}{m} p_{0_y}. \tag{3.7}$$

Note that (3.7) holds for $\phi/m \gg O(\delta^2)$. More importantly, in (3.6), which derives from (2.5), α does not have to be $O(1)$ to maintain the balance between the terms; it may be large since the Darcy term $\alpha^2 u_0$ remains $O(1)$. The reason is as follows. The pressure gradient p_x is $O(1)$ because it is the driving force. For a large α, the flow is expected to follow Darcy's law, and balancing p_x with the Darcy term in (2.5) leads to $u \sim \alpha^{-2}$. This result merely states that for large α the correct velocity scales would be $Q/b\alpha^2$ in the axial direction and $Q/L\alpha^2$ in the vertical direction. We shall later confirm this large α behaviour from the leading solution of the layer. This argument is also similar to Feng & Weinbaum (2000) for glycocalyx flow due to the motion of a red blood cell which is embedded in the compressible glycocalyx layer. Their study also pointed out that, for large α, an $O(1)$ velocity induces an $O(\alpha^2)$ pressure in the layer.

For the solid phase of the layer, the leading-order horizontal displacement u_0^s is governed by the leading order of (2.8),

$$-\alpha^2 u_0 = -\frac{1 - \phi}{m} p_{0_x} + \eta u_{0_{yy}}^s. \tag{3.8}$$

The leading-order vertical displacement v_0^s will be determined in the $O(\delta^2)$ problem.

The leading-order boundary conditions (2.10)–(2.15) are given by

$$u_0 = 0, \quad v_0 = 0 \quad \text{at} \quad y = B_i(x), \tag{3.9a, b}$$

$$u_s = 0 \quad \text{at} \quad y = B_i(x), \tag{3.10}$$

$$U_0 = \phi u_0, \quad V_0 = \phi v_0 \quad \text{at} \quad y = H_i(x), \tag{3.11a, b}$$

$$\phi U_{0_y} = m u_{0_y} \quad \text{at} \quad y = H_i(x), \tag{3.12}$$

$$(1 - \phi)U_{0_y} = m\eta u_{0_y}^s \quad \text{at} \quad y = H_i(x), \tag{3.13}$$

$$P_0 = p_0 \quad \text{at} \quad y = H_i(x). \tag{3.14}$$

With the above boundary conditions, we can solve the leading-order flow fields. Solving (3.2)–(3.4) for the leading-order core flow results in

$$U_0 = \tfrac{1}{2} P_{0_x} y^2 + A_1 y + A_2, \tag{3.15}$$

$$V_0 = \tfrac{1}{6} P_{0_{xx}} y^3 - \tfrac{1}{2} A_{1_x} y^2 - A_{2_x} y + A_3, \tag{3.16}$$

where A_1, A_2 and A_3 are constants of integration.

For the fluid phase of the glycocalyx layers, we solve (3.5)–(3.7) for the velocity field

$$u_0^i = \frac{-\phi P_{0_x}}{\alpha^2 m} + a_1^i \cosh(\alpha(y - B_i)) + a_2^i \sinh(\alpha(y - B_i)), \tag{3.17}$$

$$v_0^i = \frac{\phi}{\alpha^2 m} P_{0_{xx}}(y - B_i) + \left(a_1^i B_{i_x} - \frac{a_{2_x}^i}{\alpha} \right) \cosh(\alpha(y - B_i))$$
$$+ \left(a_2^i B_{i_x} - \frac{a_{1_x}^i}{\alpha} \right) \sinh(\alpha(y - B_i)) + b_i, \tag{3.18}$$

where a_1^i, a_2^i, and b_i are constants of integration. A_1, A_2, a_1^i, a_2^i and b_i are given by the following.

$$a_1^1 = a_1^2 = \frac{\phi}{\alpha^2 m} P_{0_x}, \quad a_2^1 = P_{0_x} f_1, \quad a_2^2 = P_{0_x} f_2,$$

$$b_1 = -a_1^1 B_{1_x} + \frac{1}{\alpha}\left(a_2^1 \right)_x, \quad b_2 = -a_1^2 B_{2_x} + \frac{1}{\alpha}\left(a_2^2 \right)_x,$$

$$A_1 = P_{0_x} F_1, \quad A_2 = P_{0_x} F_2,$$

where we define $\beta = -\alpha\epsilon$, and

$$f_1 = \frac{1}{(2\phi^2 \sinh(\beta) + m\alpha \cosh(\beta)(H_1 - H_2))}$$
$$\times \left(\frac{\phi^3 \tanh(\beta)}{\alpha^2 m}(\alpha(H_1 - H_2) + 2\sinh(\beta)) - \tfrac{1}{2}\phi\left(H_1^2 - H_2^2 \right) \right)$$
$$+ \frac{(H_1 - H_2)}{(2\phi^2 \sinh(\beta) + m\alpha \cosh(\beta)(H_1 - H_2))} \left(\frac{\phi}{\alpha} \sinh(\beta) + \phi H_1 \right),$$

$$f_2 = f_1 - \frac{\phi}{\alpha^2 m \cosh(\beta)}(\alpha(H_1 - H_2) + 2\sinh(\beta)),$$

$$F_1 = -\frac{1}{\alpha} \sinh(\beta) + \frac{m\alpha}{\phi} \cosh(\beta) f_1 - H_1,$$

$$F_2 = -\frac{\phi^2}{\alpha^2 m}(1 - \cosh(\beta)) - \phi f_1 \sinh(\beta) - \tfrac{1}{2}H_1^2 - F_1 H_1.$$

a_2^i and b_i ($i = 1, 2$) are x-dependent and can be determined using (3.9), (3.11a) and (3.12). Note that $P_0(x) = p_0(x)$ because of (3.4), (3.7) and (3.14). Also note that V_0 and v_0 are solved by applying (3.11b) at $y = H_i(x)$ and (3.9b), respectively. To evaluate unknown P_{0_x}, we consider the constant total flow rate across the channel

$$1 = \int_{H_2}^{H_1} U_0 \, dy + \phi \int_{H_1}^{B_1} u_0^1 \, dy + \phi \int_{B_2}^{H_2} u_0^2 \, dy. \tag{3.19}$$

Notice that neither the core flow rate nor the layer flow rate individually remain constants in x since the interface is permeable. This means that, as we shall see, flow streamlines can pass through the interface. Differentiating (3.19) with respect to x, and applying continuity, (3.9) and (3.11a) lead to

$$0 = \left[-V_0(y = H_1) + \phi v_0^1(y = H_1) \right] + \left[-V_0(y = H_2) + \phi v_0^2(y = H_2) \right]. \tag{3.20}$$

This is identical to (3.11b). Since we have applied (3.11b) at $y = H_1(x)$ for determining V_0, the second bracket of (3.20) (which is identical to (3.11b) at $y = H_2(x)$) is automatically satisfied. Using (3.19), we then can express P_{0_x} in terms of known functions $\hat{Q}(x)$ as

$$P_{0_x} = \frac{1}{\hat{Q}}, \tag{3.21}$$

$$\hat{Q} = \tfrac{1}{6}\left(H_1^3 - H_2^3\right) + \tfrac{1}{2}\left(H_1^2 - H_2^2\right) F_1 + (H_1 - H_2) F_2 - \frac{2\phi^2}{\alpha^2 m} \epsilon$$
$$+ \frac{\phi^2}{\alpha^3 m} \sinh(\beta) + \frac{\phi}{\alpha}(1 - \cosh(\beta)) f_1 + \frac{\phi}{\alpha}(\cosh(\beta) - 1) f_2.$$

Knowing P_{0_x}, we can determine the leading-order flow fields of both the core and the fluid phase of the poroelastic layer from (3.15)–(3.18). We would now like to examine the large α behaviour of u_0 to confirm our earlier scaling issue for (3.6). For large α, since $f_1 \sim \phi/\alpha^2 m + \phi/\alpha m\, e^{-\alpha \epsilon}(H_1 - H_2)$, we can show that $F_1 \sim -(H_1 + H_2)/2$ and $F_2 \sim H_1 H_2/2$ are $O(1)$. Then, (3.21) for large α leads to

$$P_{0_x} \sim \left(\tfrac{1}{6}\left(H_1^3 - H_2^3\right) - \tfrac{1}{4}(H_1 + H_2)\left(H_1^2 - H_2^2\right) + \tfrac{1}{2}H_1 H_2 (H_1 - H_2) \right)^{-1},$$

which is $O(1)$. Therefore (3.17) for the axial fluid velocity of the layer has an asymptotic behaviour:

$$u_0^i \sim -\frac{\phi P_{0_x}}{\alpha^2 m} \quad \text{as} \quad \alpha \gg 1. \tag{3.22}$$

This confirms our earlier scaling arguments concerning the admissibility of large α in the asymptotics. Note that (3.22) satisfies boundary conditions on neither the wall nor the interface. This implies that there are two boundary layers near the wall and the interface where viscous forces are important. The axial velocity of the core for large α is $U_0 \sim P_{0_x}(y^2 - (H_1 + H_2)y + H_1 H_2)/2$ which is $O(1)$ since the $O(1)$ pressure gradient balances the viscous term in (2.2). Further, large α behaviour for U_0 is asymptotically the same as the flow in a rigid wavy channel because layers become almost impermeable.

Using the leading-order axial velocity profile (3.17) in the glycocalyx-layer fluid phase, we now solve (3.8) with boundary conditions (3.10) and (3.13) for the leading-order axial solid displacement. The solution is given by

$$u_0^{is} = \frac{1}{2m\eta} P_{0_x} (y^2 - B_i^2) + A^{is}(y - B_i) - \frac{1}{\eta} (a_1^i \cosh(\alpha(y - B_i)) + a_2^i \sinh(\alpha(y - B_i))),$$

(3.23)

$$A^{is} = \frac{1}{m\eta} (-\phi P_{0_x} H_i + (1 - \phi)A_1 - m\alpha((-1)^{i-1} a_1^i \sinh(\beta) - a_2^i \cosh(\beta))).$$

Equation (3.23) suggests that $u_0^s \sim \eta^{-1} \sim \mu_2 Q/\mu_s b^2$. However, for the small-deformation assumption to be valid, the axial solid displacements should remain small enough within the layers so that they do not significantly disturb the flow fields at the layers. That is, $u_0^s \ll \epsilon$, i.e. $\eta \gg \epsilon^{-1}$.

3.2. The $O(\delta^2)$ problem

At $O(\delta^2)$, for $Re = O(1)$, the governing equations for the core are

$$U_{0_x} + V_{0_y} = 0,$$ (3.24)

$$Re(U_0 U_{0_x} + V_0 U_{0_y}) = -P_{1_x} + U_{1_{yy}} + U_{0_{xx}},$$ (3.25)

$$0 = -P_{1_x} + V_{0_{yy}}.$$ (3.26)

For the fluid phase in the layer,

$$u_{1_x} + v_{1_y} = 0,$$ (3.27)

$$\alpha^2 u_1 = -\frac{\phi}{m} P_{1_x} + u_{1_{yy}} + u_{0_{xx}},$$ (3.28)

$$\alpha^2 v_0 = -\frac{\phi}{m} P_{1_y} + v_{0_{yy}}.$$ (3.29)

The $O(\delta^2)$ system is subject to the following boundary conditions:

$$u_1 = 0, \quad v_1 = 0 \quad \text{at} \quad y = B_i(x),$$ (3.30)

$$U_1 = \phi u_1, \quad V_1 = \phi v_1 \quad \text{at} \quad y = H_i(x),$$ (3.31)

$$\phi(U_{1_y} + V_{0_x} - H_{i_x}^2 U_{0_y} + 2H_{i_x}(V_{0_y} - U_{0_x}))$$
$$= m(u_{1_y} + v_{0_x} - H_{i_x}^2 u_{0_y} + 2H_{i_x}(v_{0_y} - u_{0_x})) \quad \text{at} \quad y = H_i(x), \quad (3.32)$$

$$\phi(-P_1 + 2(V_{0_y} - H_{i_x} U_{0_y})) = -\phi p_1 + 2m(v_{0_y} - H_{i_x} u_{0_y}) \quad \text{at} \quad y = H_i(x).$$ (3.33)

Similar to the way we have solved the leading-order flows, we shall again apply the flow rate constraint

$$\int_{H_2}^{H_1} U_1 \, dy + \phi \int_{H_1}^{B_1} u_1^1 \, dy + \phi \int_{B_2}^{H_2} u_1^2 \, dy = 0.$$ (3.34)

The solution to (3.25) for the core is

$$U_1 = \tfrac{1}{30} E_6 y^6 + \tfrac{1}{20} E_5 y^5 + \tfrac{1}{12} E_4 y^4 + \tfrac{1}{6} E_3 y^3 + \tfrac{1}{2} E_2 y^2 + E_1 y + E_0,$$ (3.35)

where $E_0(x)$, $E_1(x)$, and $E_2(x)$ are unknowns, and

$$E_3 = Re P_{0_x} (F_2(P_{0_x} F_1)_x + A_3) - (P_{0_x} F_1)_{xx},$$

$$E_4 = \tfrac{1}{2} Re P_{0_x} (P_{0_x} F_2 + F_1(P_{0_x} F_1)_x - (P_{0_x} F_2)_x) - P_{0_{xxx}},$$

$$E_5 = \tfrac{1}{3} Re P_{0_x} P_{0_{xx}} F_1, \quad E_6 = \tfrac{1}{12} Re P_{0_x} P_{0_{xx}}.$$

For the fluids in the layers we solve (3.28) with (3.17) for the $O(\delta^2)$ axial velocity

$$u_1^1 = c_1 \cosh(\alpha(y - B_1)) + c_2 \sinh(\alpha(y - B_1)) - \frac{s_1}{2\alpha}(y - B)\sinh(\alpha(y - B_1))$$

$$- \frac{s_2}{2\alpha}(y - B)\cosh(\alpha(y - B_1)) + \frac{\phi P_{0_{xxx}}}{2m}\left(\frac{2}{\alpha^4} + \frac{y^2}{\alpha^2}\right) - \frac{d_{1_x}}{\alpha^2}y + \frac{(s_0 - e_1)}{\alpha^2}, \quad (3.36)$$

$$u_1^2 = c_3 \cosh(\alpha(y - B_2)) + c_4 \sinh(\alpha(y - B_2)) - \frac{s_3}{2\alpha}(y - B_2)\sinh(\alpha(y - B_2))$$

$$- \frac{s_4}{2\alpha}(y - B_2)\cosh(\alpha(y - B_2)) + \frac{\phi P_{0_{xxx}}}{2m}\left(\frac{2}{\alpha^4} + \frac{y^2}{\alpha^2}\right) - \frac{d_{2_x}}{\alpha^2}y + \frac{(s_0 - e_2)}{\alpha^2}, \quad (3.37)$$

where $c_1(x), c_2(x), c_3(x), c_4(x), e_1(x), e_2(x)$ are unknowns. Here, the auxiliary functions $s_0(x), s_1(x), s_2(x), s_3(x), s_4(x), d_1(x)$ and $d_2(x)$ are given by

$$s_0 = -\phi \frac{P_{0_{xxx}}}{\alpha^2 m},$$

$$s_1 = \left((a_1^1)_x - \alpha a_2^1 B_{1_x}\right)_x - \alpha B_{1_x}\left((a_2^1)_x - \alpha a_1^1 B_{1_x}\right)$$

$$s_2 = \left((a_2^1)_x - \alpha a_1^1 B_{1_x}\right)_x - \alpha B_{1_x}\left((a_1^1)_x - \alpha a_2^1 B_{1_x}\right),$$

$$s_3 = \left((a_2^2)_x - \alpha a_1^2 B_{2_x}\right)_x - \alpha B_{2_x}\left((a_1^2)_x - \alpha a_2^2 B_{2_x}\right),$$

$$s_4 = \left((a_1^2)_x - \alpha a_2^2 B_{2_x}\right)_x - \alpha B_{2_x}\left((a_2^2)_x - \alpha a_1^2 B_{2_x}\right),$$

$$d_1 = -\alpha^2 b_1 + \frac{\phi}{m}P_{0_{xx}}B_1, \quad d_2 = -\alpha^2 b_2 + \frac{\phi}{m}P_{0_{xx}}B_2.$$

The unknowns are solved by applying boundary conditions (3.30)–(3.34).

With the above $O(\delta^0)$ and $O(\delta^2)$ flow fields, the streamlines are drawn by introducing streamfunctions for the core and the layer, respectively:

$$U = -\Psi_y, \quad V = \Psi_x, \quad (3.38)$$

$$u = -\psi_y, \quad v = \psi_x. \quad (3.39)$$

We also expand the streamfunctions in δ^2 similar to (3.1). The streamfunctions at each order are then obtained by integrating the corresponding axial velocities with respect to y.

For the solid displacements, since we expect the $O(\delta^0)$ axial solid displacement to be rather small compared to the layer thickness, the $O(\delta^0)$ vertical and the $O(\delta^2)$ axial displacements are even smaller. In addition, we also lack knowledge of $\chi = \lambda_s/\mu_s$ for solving the $O(\delta^2)$ problem for the solid displacements. We thus do not pursue it any further.

4. Results and discussion

We have applied biphasic theory for solving the flows up to $O(\delta^2)$. We here assume that the core fluid and layer fluid have matched viscosity ($m = 1$). For physiological applications the solid fraction of the glycocalyx layer is usually approximately 1%, so we assume $\phi = 0.99$ throughout. Then the system depends on the remaining parameters $\delta, \epsilon, \alpha, a, \Phi$ and Re. We first examine the case for the Stokes ($Re = 0$) core flow in a symmetric wavy channel ($\Phi = \pi$). The streamlines are shown in figure 2(a). Notice that streamlines pass through the permeable interface between the fluid and the porous medium. As mentioned earlier, this can be seen from (3.21), which states
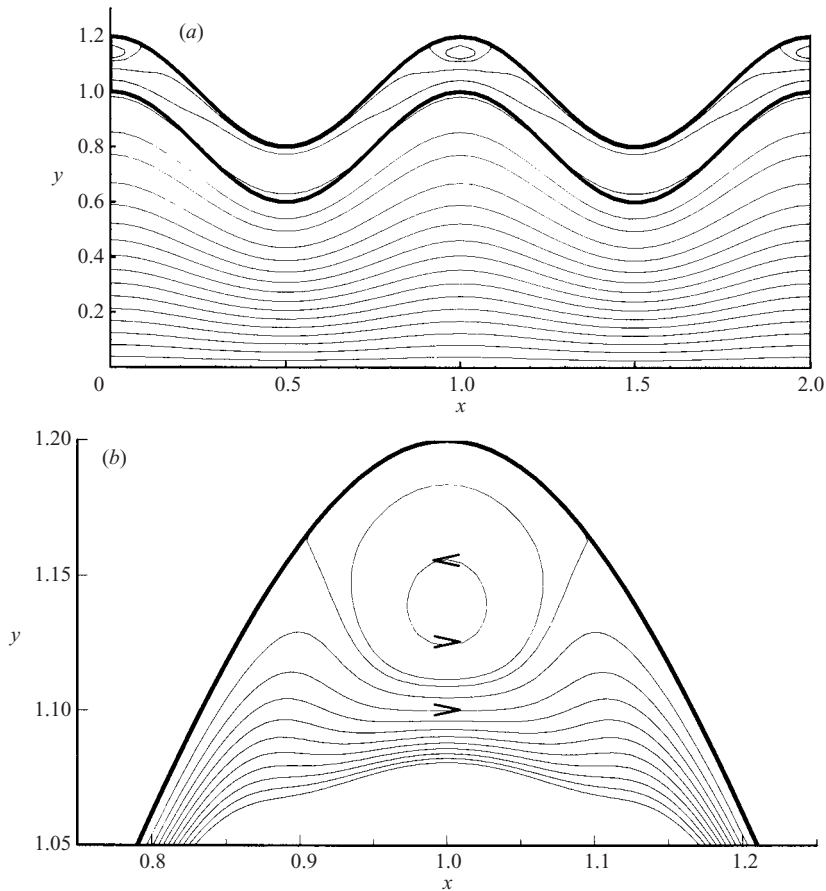
FIGURE 2. (a) The streamlines for $\alpha = 50$, $\delta = 0.3$, $\epsilon = 0.2$, $a = 0.2$, $Re = 0$ and $\Phi = \pi$. Thick solid lines are the wall (upper) and the interface (lower). The flow is left to right. (b) The streamlines within the layer in the vicinity of the widest part of the channel. Parameters are the same as (a).

that total flow rate across the channel is constant, but the flow rate across each phase is not. The flow separates in the layer region at the widest part of the channel. The separation is symmetrical about the wall's valley because the Stokes flow is reversible. This flow separation arises from $O(\delta^2)$ effects, since the leading-order flow follows the geometry of the wall. Figure 2(b) is a close-up view of the standing vortex in the valley. This trapped recirculation of the fluid increases residence time of particles near the valley and is thus potentially critical to the mass transport of dissolved substances which pass through/across cell–cell junctions. However, lining cells along the capillary may not necessarily form symmetric configurations. Figure 3 shows the streamlines for the wall-phase difference $\Phi = 0.8\pi$ (figure 3a), 0.5π (figure 3b) and 0 (figure 3c). In comparison with figure 2 for a symmetric case $\Phi = \pi$, the recirculation becomes smaller and starts to move upstream for $\Phi = 0.8\pi$. Further decreasing Φ, making the walls more in-phase, causes recirculation to disappear. The mechanism of flow separation is explained below.

The flow separation can be interpreted more easily in terms of the corresponding axial velocities, as shown in figure 4 for a symmetric channel. We plot the layer
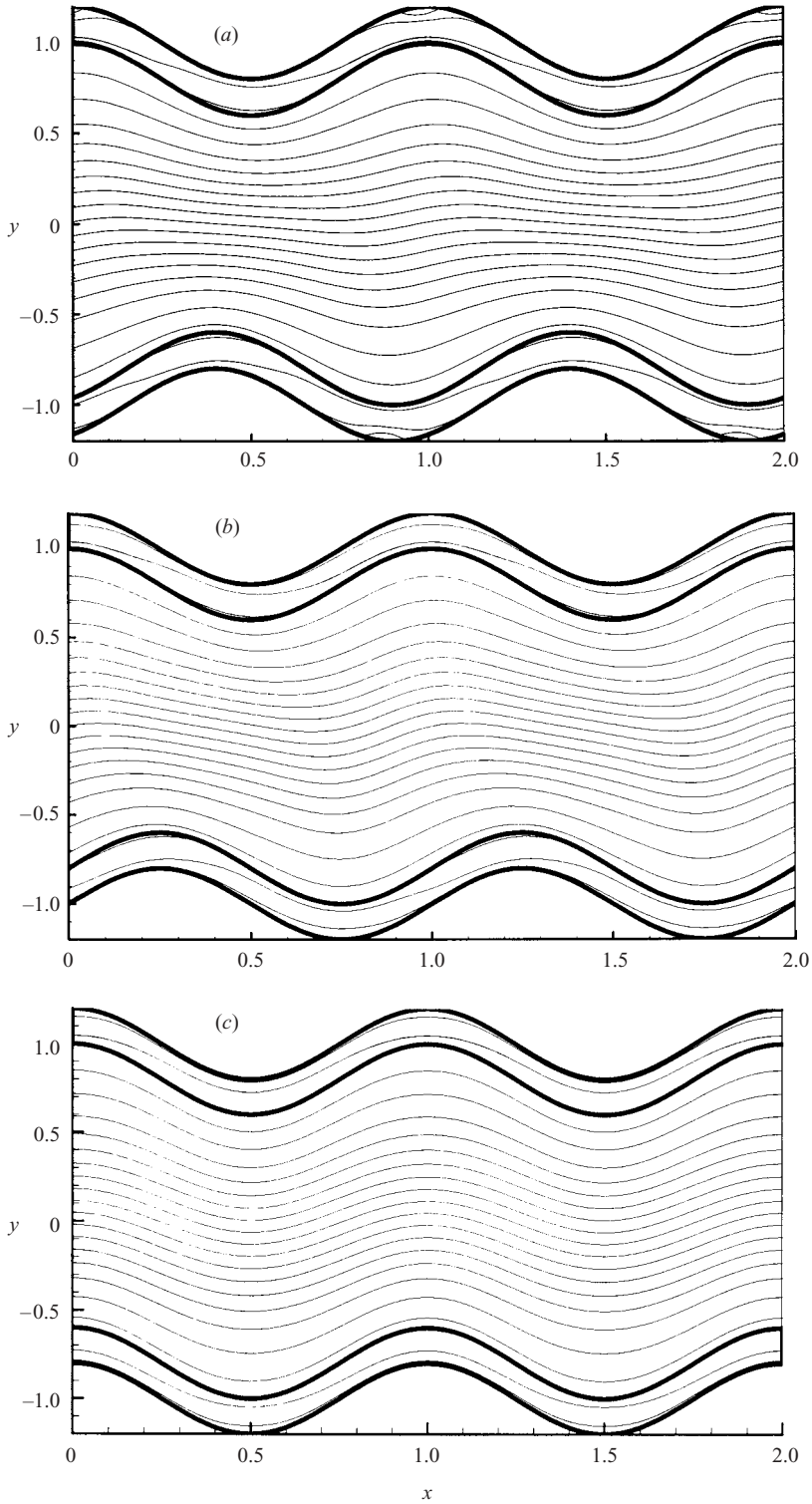
FIGURE 3. The streamlines for $\alpha = 50$, $\delta = 0.3$, $\epsilon = 0.2$, $a = 0.2$ and $Re = 0$. (*a*) $\Phi = 0.8\pi$, (*b*) $\Phi = 0.5$, π (*c*) $\Phi = 0$. The flow is left to right.
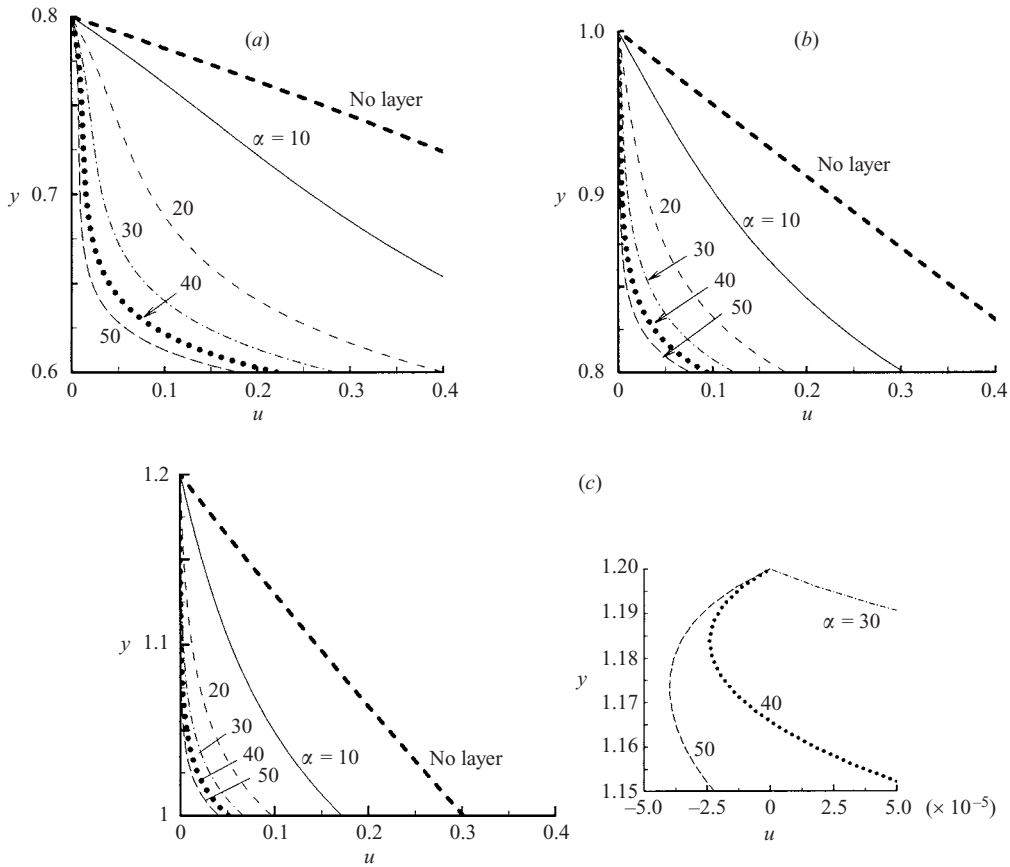
FIGURE 4. The corresponding axial velocity profile in the layer for figure 2. (*a*) $x = 0.5$, (*b*) $x = 0.75$. For (*c*), the right-hand figure is an enlarged view for the small u regime at $x = 1$.

velocities at three different axial locations: at the crest $x = 0.5$ (figure 4*a*), $x = 0.75$ (figure 4*b*) and at the valley $x = 1.0$ (figure 4*c*). At all locations, increasing α reduces the layer flow speed because of decreasing permeability. For large α we recall that $u \sim \alpha^{-2}$ and the velocity becomes more uniform across the layer, where Darcy's flow dominates, except near the interface and the wall where viscous layers are developed. In figure 4(*c*), the flow starts to reverse when α is large enough, as shown in the enlarged view. We also calculate that no flow separation occurs in the absence of the layer. This agrees with the creeping flow analysis in a wavy channel (Pozrikidis 1987). The flow separation can be identified by a sign change in vorticity or wall shear stress. Figure 5 shows the wall stress distributions for various α in a symmetric channel. In the absence of the layer, the wall stress is largest where as the presence of the layer reduces the wall stress. For a smaller α, the wall stress is positive throughout, indicating no flow separation. Clearly, the magnitude of the wall stress decreases with increasing α because of slower velocities. For $\alpha \geqslant 40$, the wall stress changes sign over a small region near $x = 1$, as shown in the enlarged view, indicating flow separation. Further increases in α increase the size of the recirculation.

All the above suggests that large α favours flow separation. Slow fluid motions of the layer owing to large α result in small wall shear magnitudes so that effects of $O(\delta^2)$ stress modifications can be sufficient to reverse the sign. Recall that a non-symmetric
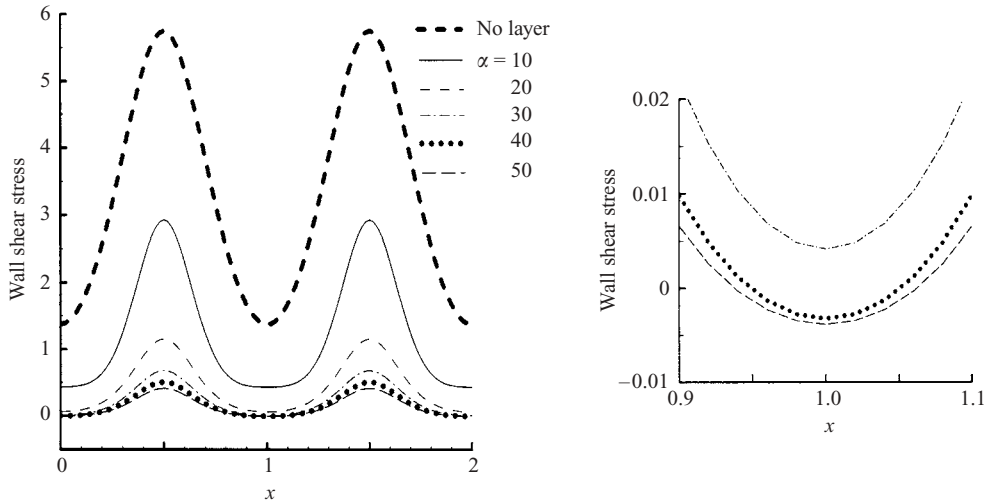
FIGURE 5. The wall stress distributions for various α. $\delta = 0.3$, $\epsilon = 0.2$, $a = 0.2$, $Re = 0$ and $\Phi = \pi$. The right-hand figure is an enlarged view for the small wall stress regime near $x = 1$.
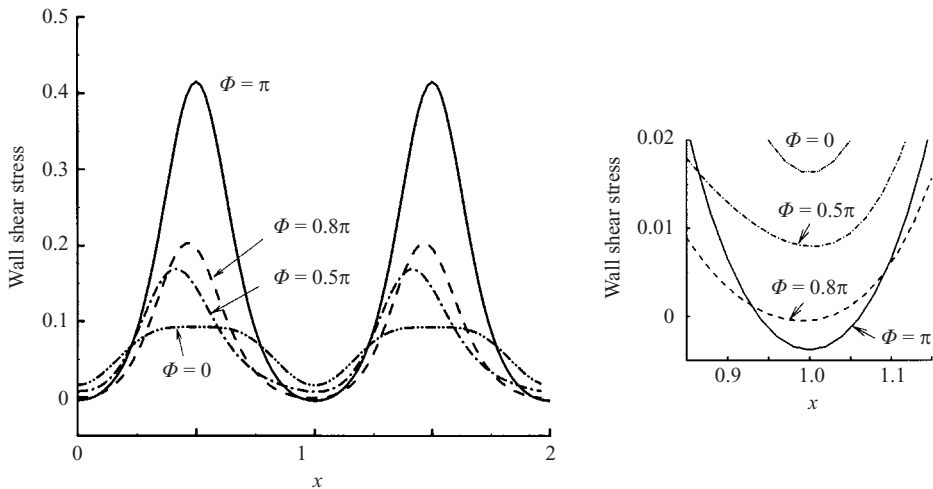

FIGURE 6. The top wall stress distribution for various Φ. $\alpha = 50$, $\delta = 0.3$, $\epsilon = 0.2$, $a = 0.2$ and $Re = 0$. The right-hand figure is an enlarged view for the small wall stress regime.

channel diminishes the recirculation, as shown in figure 3. Observing the case of $\Phi = 0.8\pi$ in figure 3(a), the widest parts of the channel are located at $x \approx 0.9$ ahead of those of a symmetric channel. This explains that the recirculation shifts upstream. However, the widest parts of the channel are smaller than those of a symmetric case. It thus diminishes the size of the recirculation. When further decreasing Φ, the widest parts of the channel become even smaller and thus hardly trigger flow separations.

To justify the above, we examine the effect of the wall phase on the top wall shear stress, as shown in figure 6. At first glance, decreasing Φ from π decreases the wall stress. For $\Phi = 0.8\pi$ however, the minimum wall stress is less negative than $\Phi = \pi$; but the location of the minimum wall stress slightly shifts to upstream. These support the appearance of recirculation, as shown in figure 3(a). The wall stresses of $\Phi = 0.5\pi$ and
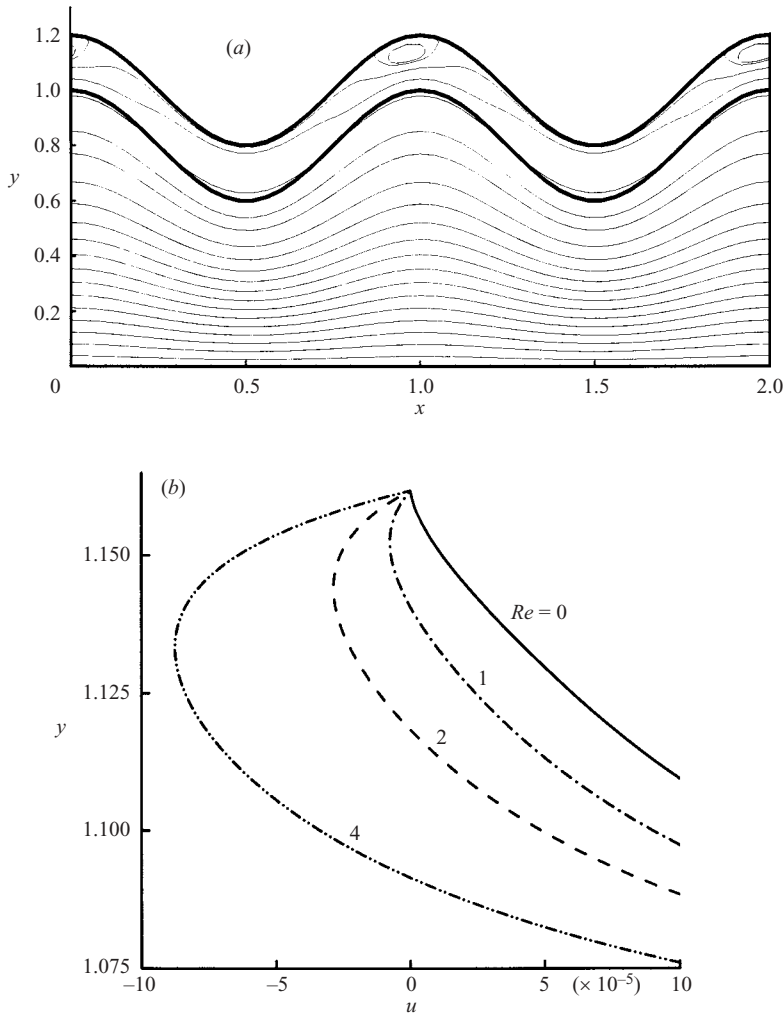
FIGURE 7. (*a*) The streamlines for $\delta = 0.3$, $\epsilon = 0.2$, $a = 0.2$, $Re = 2.0$, $\alpha = 50$ and $\Phi = \pi$. The flow is from left to right. (*b*) The layer axial velocity profile near the wall at $x = 0.9$. $\delta = 0.3$, $\epsilon = 0.2$, $a = 0.2$, $\alpha = 50$ and $\Phi = \pi$.

0 become positive everywhere along the wall. These verify the streamlines observed in figure 3.

Further, we should expect that the larger α is, the smaller the wall amplitude or the longer the wavelength required to cause flow separation. However, flow separations are less likely for a thinner layer because the velocity gradient becomes steeper and is more favourable to keeping the fluid moving forward.

The above discussion for the flow recirculation is for $Re = 0$ core flow. The core's inertia, however, is expected to change recirculation patterns in the layer. We again use the symmetric channel case to illustrate the inertial effect of the core on the flow separation. Figure 7(*a*) shows the corresponding streamlines. In comparison with figure 2, the flow separation shifts upstream. When the flow starts to pass wider parts of the channel, the core's inertia tends to establish an adverse pressure gradient to reverse the flow. Even though the layer fluid does not have inertia, the tendency of the core flow reversal is transmitted, via the continuous interfacial velocities and shear

stresses, through the layer so that the wall stress is further reduced and the layer flow begins to separate. The shift of the flow separation upstream is thus anticipated for non-zero Reynolds numbers. It also qualitatively agrees with the study in two immiscible Newtonian fluids flowing in a core–annular configuration with slowly varying cross-sections (Kouris & Tsamopoulos 2000). Figure 7(b) shows the core inertial effect on the layer axial velocity distributions at $x = 0.9$ near the valley. The above flow recirculation shifting upstream would be a small effect in a capillary because $Re \ll 1$. It, however, at least describes qualitatively what happens for flows in larger blood vessels when the inertia is important. In this case, molecules probably reside around cell junctions which are susceptible to some artery disease (Yuan, Chien & Weinbaum 1991).

We now examine the pressure distribution within the layer. Local pressures together with shear stresses on cell membranes may trigger cellular responses to stress (Satcher *et al.* 1992). The pressure gradient in the layer determines the flow direction, as dictated by the biphasic theory. To leading order, there is only an axial pressure gradient and it is always negative, so no recirculation occurs. However, at $O(\delta^2)$ the transverse pressure gradient becomes non-zero and varies in sign in the recirculation region. At the same order, the axial gradient can achieve positive values in this region, thereby yielding the predicted recirculation. Figure 8(a) shows the pressure distribution along the wall for different axial positions in a symmetric channel. As expected, a higher α steepens overall pressure drop because of a lower permeability. The pressure slightly increases near the wall's valley ($x = 1$), indicating that an adverse pressure is developed. The corresponding pressure gradient is shown in figure 8(b) and is slightly positive near the valley. This pressure gradient near the valley increases with increasing α for $\alpha \gtrsim 30$. Recall that the flow separation occurs for $\alpha \gtrsim 40$. It suggests that adverse pressure is not strong enough to cause a flow reversal until $\alpha \sim 40$. For non-symmetric channels, since the wall stresses are smaller then they symmetric channel, as shown in figure 6, the corresponding pressure gradients are less steep than that of the symmetric channel.

We have taken solids into account using the biphasic theory for the poroelastic layer. Figure 9 shows the distribution of the leading-order axial solid displacement at particular axial position for a symmetric channel. Recall that the solid displacement is dictated by the flow field. Also notice again that $\eta \gg \epsilon^{-1}$ is required for the small-solid-deformation assumption to remain valid. Here, we choose $\eta = 100$, displacement is $O(10^{-3})$ which is much smaller than the layer thickness of 0.2. The solid displacement increases as the permeability decreases. For a larger α, larger pressure gradient is required to drive the fluid phase through the solid matrix, enlarging the deformation of the solid phase. Alternatively, because the shear stress in the fluid phase becomes smaller for a larger α, as evidenced by the axial velocity profiles in figure 4, a larger portion of the stress must be exerted by the solid phase. Thereby, the deformation of the solid phase increases with α.

According to the biphasic theory, the contribution of the solid to the flow field is effectively reflected by $(1 - \phi)$ the volume fraction of the solid. Notice that from (3.7), ϕ/m remains $O(1) \gg \delta^2$ in order to preserve the small variation of the pressure across the layer in the leading order. This means that the solid phase cannot be too dense in the mixture. An allowable range of the solid fraction is roughly $0.01 \sim 0.1$ which is consistent with physiological values. As our results show, within an allowable range of solid fractions, the solid phase does not change the flow field significantly. We thus conclude that the major factor that affects the flow patterns is the permeability, particularly when the permeability is low enough.
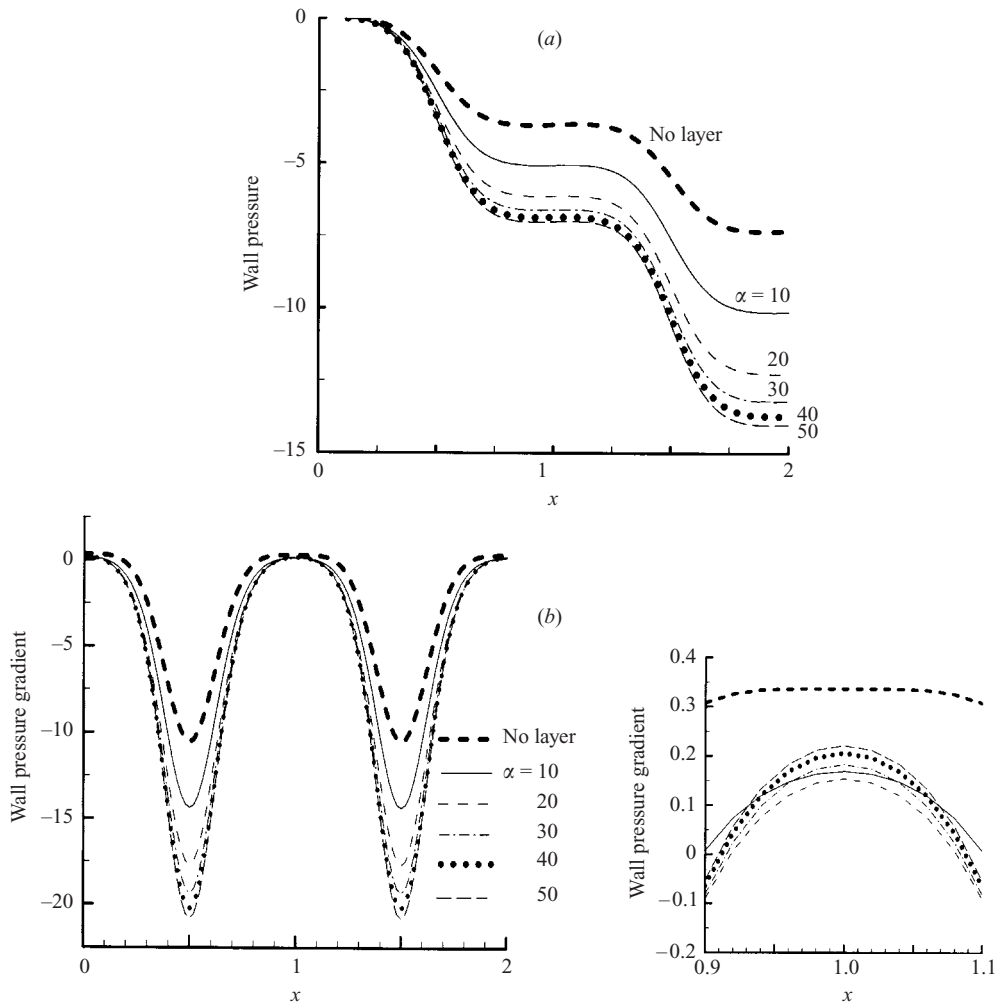
FIGURE 8. (*a*) The wall pressure distribution for various α. $\delta = 0.3$, $\epsilon = 0.2$, $a = 0.2$, $Re = 0$ and $\Phi = \pi$. (*b*) The wall pressure gradient corresponding to (*a*).

We now turn our attention to the flow rate across the glycoaclyx layers. Since fluid is allowed to penetrate through the permeable core–layer interface, the flow rate across the layer is not constant. The flow rate in the layer Q_L is evaluated by the streamfunction difference between the wall and the streamline that gives the maximum flow rate within the layer. We are also interested in the flow rate Q_{CL} that moves between the core and the layer because it relates to transport of molecules that can enter and exit the layer. Q_L and Q_{CL} are expressed as percentages of the total flow rate in figure 10 where we examine the effect of the wall phase Φ. Figure 10 shows that increasing Φ causes Q_L to decrease. This is because the flow resistance in the layer increases, as suggested in figure 6, for the wall stress distribution. However, increasing Φ promotes Q_{CL}. This can be realized as follows. When the walls are close to the in-phase configuration, all streamlines are expected to be in phase with the walls. This reduces the tendency for the stream to enter or leave the layer. Furthermore, Q_{CL} is higher than Q_L. Even though the cross-sectional area for Q_{CL} is smaller than that for Q_L, the velocity in the Q_{CL} region is much faster than the layer, recall that most
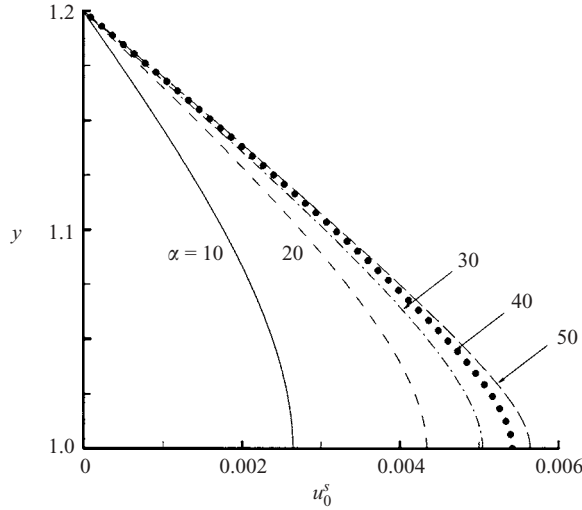
FIGURE 9. The distribution of leading-order axial displacement of a solid at $x = 1$ for various α. $\delta = 0.3$, $\epsilon = 0.2$, $a = 0.2$, $Re = 0$ and $\Phi = \pi$.
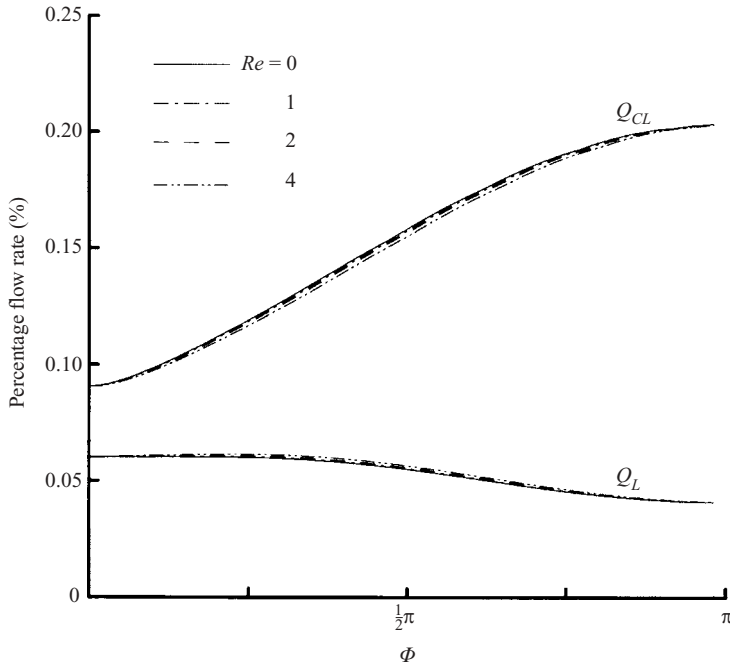

FIGURE 10. The effect of the wall phase Φ on the percentage flow rate. Percentage flow rates that move between the core and the layer are Q_{CL}. Those within the layer are Q_L. $\epsilon = 0.2$, $a = 0.2$, $\delta = 0.3$ and $\alpha = 50$.

of layer velocities are small for large α as shown in figure 4. Both Q_L and Q_{CL} are less sensitive to the effect of the core inertia. Increasing Re slightly decreases Q_L and increases Q_{CL}.

Figure 11(a) shows the effect of the wall phase Φ on the normal velocity on the core–layer interface $V_n = \boldsymbol{v} \cdot \boldsymbol{n}$. Note that $V_n(\Phi = 0)$ is not zero, but small ($O(10^{-6})$).
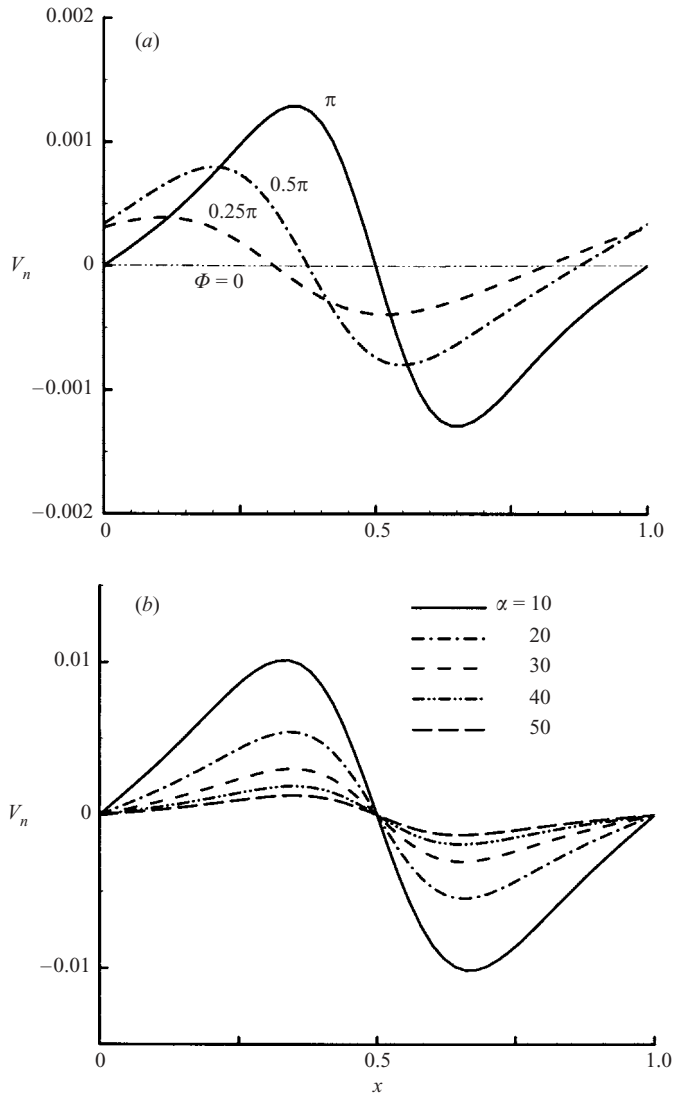
FIGURE 11. (a) The effect of the wall phase Φ on the normal core–layer interface velocity V_n. $\delta = 0.3$, $\epsilon = 0.2$, $a = 0.2$ and $Re = 0$. (b) The effect of the wall phase α on the normal core–layer interface velocity V_n. $\delta = 0.3$, $\epsilon = 0.2$, $a = 0.2$, $Re = 0$ and $\Phi = 0.5\pi$.

Increasing Φ increases V_n because the less in-phase streamlines have a stronger tendency to enter or leave the layer. This also supports the behaviour of Q_{CL} in figure 10. The effect of α on V_n for a symmetric channel is shown in figure 11(b). Increasing α also decreases V_n since the layer is less permeable and the resistance becomes larger.

5. Physiological applications and conclusions

The radius of a capillary is between 2.5 and 5 μm. The length of an endothelial cell is 20–50 μm. Thus, the aspect ratio for a capillary δ is between approximately 0.05 and 0.3. The mean velocity of blood in capillaries is 7.5×10^{-2} cm s^{-1}. The blood is

assumed to be a homogeneous Newtonian fluid of density $1.05\,\mathrm{g\,cm^{-3}}$ and viscosity 0.01 poise. The typical Reynolds number is thus of the order of 10^{-2}.

The average thickness of the cells is $1\text{--}2\,\mu\mathrm{m}$ (Satcher *et al.* 1992). The amplitude of the endothelial membrane variations is approximately $1.5\,\mu\mathrm{m}$ (Barbee, Davies & Lal 1994) and the corresponding dimensionless wall amplitude is between 0.2 and 0.6. The thickness of the glycocalyx in capillaries is $200\text{--}400\,\mathrm{nm}$ (Gretz 1995) up to $1\,\mu\mathrm{m}$ (Silberberg 1991; Turner, Clough & Michel 1983). Hence, the dimensionless wall-layer thickness ϵ is around 0.2.

The glycoclayx is composed primarily of glycoproteins and proteoglycans and also adsorbs plasma proteins, such as fibrinogen and albumin. There are no direct measurements for the Darcy permeability K_p within the layer. Estimates in other biological materials have a wide range. K_p is $10^{-10}\,\mathrm{cm^{-2}}$ for mesentery (Levick 1987). A fibre-matrix model (Tsay & Weinbaum 1991) estimates K_p to be about $10^{-13}\,\mathrm{cm^{-2}}$ for fibres with diameter $1\,\mathrm{nm}$ and spacing $7\,\mathrm{nm}$ (as a molecular sieve to albumin). Hence, K_p ranges from 10^{-13} to $10^{-10}\,\mathrm{cm^2}$ and the corresponding dimensionless hydraulic resistivity varies as $10 \leqslant \alpha \leqslant 10^3$. The solid component is usually less than 1% and we thus choose $\phi = 0.99$. Therefore, these parameters are within the ranges to which our present model is applied.

We employ a model using biphasic theory not only to access the effective influence of the porous medium, but also the elastic behaviour of the solid composition. We solve pressure-driven flows for both the core and the layer using the lubrication approximation in the small aspect ratio δ. The flow fields are solved up to $O(\delta^2)$. A striking finding is that the existence of a porous layer may result in the formation of trapped recirculation within the layer, depending on the range of the parameters such as permeability and the wall phase difference, and this vortex is located in proximity to the intercellular clefts where transendothelial transport occurs. Flow recirculation does not occur at these parameter values if the layer is absent. It is more feasible for a layer with low permeability. Our detailed analysis reveals that a layer with a low permeability reduces the wall shear stresses so that the flow is more vulnerable to adverse pressures. A consequence of recirculation is to increase residence times of circulating substances around cell junctions that are susceptible to some arterial diseases. However, for larger blood vessels, an increase in the Reynolds number leads the recirculation to move upstream, which may influence the disease process.

The wavy geometry allows the stream to enter and exit the layer, which provides a mechanism for convective transport between these two regions that otherwise have only diffusive interactions. The estimated normal velocity $V_n^* = \boldsymbol{v}^* \cdot \boldsymbol{n}$ across the core–layer interface is about $10^{-4}\,\mathrm{cm\,s^{-1}}$ for $K_p \sim 10^{-10}\,\mathrm{cm^2}$. The corresponding Péclet number $Pe = V_n^* b / D$, where D is the molecular diffusivity, ranges from $O(10^{-2})$ to $O(10)$ for D from 10^{-6} to $10^{-9}\,\mathrm{cm^2\,s^{-1}}$. This suggests that the convective transport is important for large molecules where $D < 10^{-8}\,\mathrm{cm^2\,s^{-1}}$. Though a large molecule such as albumin normally does not enter the intercellular clefts, it may penetrate the intercellular clefts when malfunctioned or diseased cells cause a wider cell–cell junction which may allow a large molecule to pass through it, e.g. atherosclerosis (Lin *et al.* 1988). Therefore, our model at least provides an estimation for the transport of large molecules occurring in the above situation.

The contribution of solid to the flow system is only reflected by the solid fraction. However, within the range of applications, the solid composition does not significantly change the flow patterns. The solid displacements are determined solely by the flow field and are much smaller than the layer thickness. The result reveals that the lower the permeability, the larger the solid deformation. When red cells are present, the

layer is expected to be highly compressed, which could result in amplification of the solid deformation so that the interaction between the solid and fluid phases is no longer as simple as in our present study. Clearly, in this case the permeability could vary in space and changes the flow characteristics significantly (Feng & Weinbaum 2000).

Appendix. Biphasic mixture theory

Governing equation in the porous medium

Let $\boldsymbol{v}$ stand for the fluid velocity inside the porous material, $\boldsymbol{u}_s$ is the solid displacement vector and $\dot{\boldsymbol{u}}_s$ is the solid velocity. The volume fraction of the fluid is ϕ. The equation of the fluid mass derived by (Mow *et al.* 1980) gives

$$\nabla \cdot (\phi \boldsymbol{v}) = 0. \tag{A 1}$$

Assuming constant ϕ reduces (A 1) to the equation of continuity. Assuming infinitesimal solid deformation in the porous material, and negligible inertia, then the momentum equation for the fluid and solid phases are

$$\nabla \cdot \boldsymbol{T}^f + k(\dot{\boldsymbol{u}}_s - \boldsymbol{v}) = 0, \tag{A 2}$$
$$\nabla \cdot \boldsymbol{T}^s - k(\dot{\boldsymbol{u}}_s - \boldsymbol{v}) = 0, \tag{A 3}$$

where $\boldsymbol{T}^f$ and $\boldsymbol{T}^s$ are the stress tensors for fluid and solid phases respectively, $k = \mu_f / K_p$ is the hydraulic resistivity with μ_f the fluid viscosity and K_p the Darcy permeability of the porous material. The stress tensors are constituted as

$$\boldsymbol{T}^f = -\phi p \boldsymbol{I} + \mu_f (\nabla \boldsymbol{v} + \nabla \boldsymbol{v}^T), \tag{A 4}$$
$$\boldsymbol{T}^s = -(1 - \phi) p \boldsymbol{I} + \chi \nabla \cdot \boldsymbol{u}_s \boldsymbol{I} + \mu_s (\nabla \boldsymbol{u}_s + \nabla \boldsymbol{u}_s^T), \tag{A 5}$$

where p is the volume-averaged pressure, $\boldsymbol{I}$ is the identity matrix, χ is a Lame coefficient and μ_s is a shear modulus of the solid phase.

Conditions at the interface between the porous medium and a pure fluid

Hou *et al.* (1989) derived boundary conditions below at the interface between the porous medium and a pure fluid. Let $\boldsymbol{V}$ denote the velocity of a pure fluid. The conservation of the fluid mass flux across the interface, and the assumption of continuous volume-averaged velocity in the tangential direction give, respectively,

$$\phi \boldsymbol{n} \cdot (\boldsymbol{v} - \dot{\boldsymbol{u}}^s) = \boldsymbol{n} \cdot (\boldsymbol{V} - \dot{\boldsymbol{u}}^s), \tag{A 6}$$
$$\phi \boldsymbol{t} \cdot (\boldsymbol{v} - \dot{\boldsymbol{u}}^s) = \boldsymbol{t} \cdot (\boldsymbol{V} - \dot{\boldsymbol{u}}^s), \tag{A 7}$$

where $\boldsymbol{n}$ and $\boldsymbol{t}$ are the unit normal and tangential of the interface, respectively. The stress boundary conditions at the interface are

$$\boldsymbol{n} \cdot (\boldsymbol{T}^f + \boldsymbol{T}^s) = \boldsymbol{n} \cdot \boldsymbol{\tau}, \tag{A 8}$$

where $\boldsymbol{\tau} = -P\boldsymbol{I} + \mu_c (\nabla \boldsymbol{V} + \nabla \boldsymbol{V}^T)$ is the stress tensor of a pure fluid with the viscosity μ_c and pressure P. A further assumption made for the stress distribution between the fluid and solid phases in the porous medium is

$$\frac{T_{nt}^f}{T_{nt}^s} = \frac{T_{nn}^f}{T_{nn}^s} = \frac{\phi}{(1 - \phi)}, \tag{A 9}$$

where $T_{nt} = \boldsymbol{n} \cdot \boldsymbol{T} \cdot \boldsymbol{t}$ and $T_{nn} = \boldsymbol{n} \cdot \boldsymbol{T} \cdot \boldsymbol{n}$ are the tangential and normal components of the stress on the interface, respectively. Equation (A 9) means that the proportion of the total stress in the porous medium borne by each phase is proportional to its volume fraction. Using (A 9), the stress condition (A 8) can be expressed as

$$\boldsymbol{n} \cdot \boldsymbol{T}^f = \phi \boldsymbol{n} \cdot \boldsymbol{\tau}, \tag{A 10}$$

or

$$\boldsymbol{n} \cdot \boldsymbol{T}^s = (1 - \phi) \boldsymbol{n} \cdot \boldsymbol{\tau}. \tag{A 11}$$

REFERENCES

ADAMSON, R. H. & CLOUGH, G. 1992 Plasma proteins modify the endothelial cell glycocalyx of frog mesenteric microvessels. *J. Physiol. Lond.* **445**, 473–486.

BARBEE, K. A., DAVIES, P. F. & LAL, R. 1994 Shear stress-induced reorganization of the surface topography of living endothelial cells imaged by atomic force microscopy. *Circ. Res.* **74**, 163–171.

BRINKMAN, H. C. 1947 A calculation of the viscous force exerted by a flowing fluid in a dense swarm of particles. *Appl. Sci. Res.* A **1**, 27.

DAMIANO, E. R. 1998 The effect of the endothelial-cell glycocalyx on the motion of red blood cells through capillaries. *Microvascular Res.* **55**, 77–91.

DAMIANO, E. R., DULING, B. R., LEY, K. & SHALAK, T. C. 1996 Axisymmetric pressure-driven flow of rigid pellets through a cylindrical tube lined with a deformable porous wall layer. *J. Fluid Mech.* **314**, 163–189.

DESJARDINS, C. & DULING, B. R. 1987 Microvessel hematocrit: measurement and implications for capillary oxygen transport. *Am. J. Physiol. (Heart Circ. Physiol. 21)* **252**, H494–H503.

FAHRAEUS, R. 1928 Die Strömungsverhältnisse und die Verteilung der Blutzellen im Gefässsyetem. Zur Frage der Bedeutng der intravaculären Erythrocytenaggregation. *Klin. Wochenschr.* **7**, 100–106.

FENG, J. & WEINBAUM, S. 2000 Lubrication theory in highly compressible porous media: the mechanics of skiing, from red cells to humans. *J. Fluid Mech.* **422**, 281–317.

GRETZ, J. E. 1995 The role of capillary anatomical and functional dimensions in capillary tube hematocrit variability. PhD thesis, University of Virginia, Charlottesville, VA.

HENRY, C. B. & DULING, B. R. 1999 Permeation of the luminal capillary glycocalyx is determined by hyaluronan. *Am. J. Physiol.* **277**, H508–H514.

HOU, J. S., HOLMES, M. H., LAI, W. M. & MOW, V. C. 1989 Boundary conditions at the cartilage–synovial fluid interface for joint lubrication and theoretical verifications. *J. Biomech. Engng* **111**, 78–87.

KOURIS, C. & TSAMOPOULOS, J. 2000 Concentric core–annular flow in a circular tube of slowly varying cross-section. *Chem. Engng Sci.* **55**, 5509–5530.

LEVICK, J. R. 1987 Flow through interstitium and other fibrous matrices. *Q. J. Exp. Physiol.* **72**, 409–438.

LIN, S. J., JAN, K. M., SCHUESSLER, G., WEINBAUM, S. & CHIEN, S. 1988 Enhanced macromolecular permeability of aortic endothelial-cells in association with mitosis. *Atherosclerosis* **73**, 223–232.

MIDDLEMAN, S. 1998 *An Introduction to Fluid Dynamics*. John Wiley.

MOW, V. C., KUEI, S. C., LAI, W. M. & ARMSTRONG, C. G. 1980 Biphasic creep and stress relaxation of articular cartilage in compression: theory and experiments. *J. Biomech. Engng* **102**, 73–84.

POZRIKIDIS, C. 1987 Creeping flow in two-dimensional channels. *J. Fluid Mech.* **180**, 495–514.

POZRIKIDIS, C. 1988 The flow of a liquid-film along a periodic wall. *J. Fluid Mech.* **188**, 275–300.

PRIES, A. R., SECOMB, T. W., GESSNER, T., SPERANDIO, M. B., GROSS, J. F. & GAEHTGENS, P. 1994 Resistance to blood flow in microvessels in vivo. *Circ. Res.* **75**, 904–915.

PRIES, A. R., SECOMB, T. W., JACOBS, H., SPERANDIO, M., OSTERLOH, K. & GAEHTGENS, P. 1997 Microvascular blood flow resistance: role of endothelial surface layer. *Am. J. Physiol. (Heart Circ. Physiol. 42)* **273**, H2272–H2279.

SATCHER, R. L. J., BUSSOLARI, S. R., GIMBRONE, M. A. J. & DEWEY, C. F. J. 1992 The distribution of fluid forces on model arterial endothelium using computational fluid dynamics. *J. Biomech. Engng* **114**, 309–316.

SECOMB, T. W., HSU, R. & PRIES, A. R. 1998 A model for red blood cell motion in glycocalyx-lined capillaries. *Am. J. Physiol. (Heart Circ. Physiol.)* **43**, H1016–H1022.

SECOMB, T. W., HSU, R. & PRIES, A. R. 2002 Blood flow and red blood cell deformation in nonuniform capillaries: effects of the endothelial surface layer. *Microcirculation* **9**, 189–196.

SECOMB, T. W., SKALAK, R., OZKAYA, N. & GROSS, J. F. 1986 Flow of axisymmetric red blood cells in narrow capillaries. *J. Fluid Mech.* **163**, 405–423.

SILBERBERG, A. 1991 Polyelectrolytes at the endothelial cell surface. *Biophys. Chem.* **41**, 9–13.

TOZEREN, H. & SKALAK, R. 1978 The steady flow of closely fitting incompressible elastic spheres in a tube. *J. Fluid Mech.* **87**, 1–16.

TSAY, R. & WEINBAUM, S. 1991 Viscous flow in a channel with periodic cross-bridging fibres: exact solutions and Brinkman approximation. *J. Fluid Mech.* **38**, 75–96.

TURNER, M. R., CLOUGH, G. & MICHEL, C. C. 1983 The effects of cationised ferritin and native ferritin upon the filtration coefficient of single frog capillaries. Evidence that proteins in the endothelial cell coat influence permeability. *Microvascular Res.* **25**, 205–222.

VINK, H. & DULING, B. R. 1996 Identification of distinct luminal domains for macromolecules, erythrocytes and leukocytes within mammalian capillaries. *Circ. Res.* **71**, 581–589.

WANG, H. & SKALAK, R. 1969 Viscous flow in a cylindrical tube containing a line of spherical particles. *J. Fluid Mech.* **38**, 75–96.

WANG, W. & PARKER, K. H. 1995 The effect of deformable porous surface layers on the motion of a sphere in a narrow cylindrical tube. *J. Fluid Mech.* **283**, 287–305.

WATERS, S., LIU, S. & GROTBERG, J. 1997 Flow over glycocalyx covered endothelial cells. *Bull. Am. Phys. Soc.* **42**, 2241.

WEINBAUM, S. 1998 1997 Whitaker distinguished lecture: models to solve mysteries in biomechanics at the cellular level; a new view of fiber matrix layers. *Ann. Biomed. Engng* **26**, 627–643.

WEINBAUM, S., TSAY, R. & CURRY, R. E. 1992 A three-dimensional junction-pore-matrix model for capillary permeability. *Microvascular Res.* **44**, 85–111.

YUAN, F., CHIEN, S. & WEINBAUM, S. 1991 A new view of convective–diffusive transport processes in the arterial intima. *J. Biomech. Engng* **113**, 314–329.